

Efficiency of single-well geothermal systems with multi-lateral drills

Selçuk Erol^{a,b,*}, Virginie Harcouët-Menou^b, Ben Laenen^b, Peter Bayer^c

^a Petroleum and Natural Gas Engineering Department, Middle East Technical University (METU), Ankara, Turkey

^b Flemish Institute for Technological Research (VITO), Boeretang 200, 2400 Mol, Belgium

^c Department of Applied Geology, Martin Luther University of Halle-Wittenberg, Halle, Germany

ARTICLE INFO

Keywords:

Single-well
Geothermal sidetracked multi-lateral wells
Numerical model
Analytical solution

ABSTRACT

Drilling costs, induced seismicity, scaling and corrosion, emissions, and assessment of the inherent uncertainty associated with the reservoir properties for long-term sustainable provision of thermal energy are the major challenges of deep geothermal systems. In particular, the cost of drilling typically comprises 50–70 % of the total capital investment of a geothermal power plant. As drilling costs are definitive for the accomplishment of deep geothermal systems, the concept to use one single drill hole for extraction and injection is arisen to reduce the overall drilling costs. The aim of this study is to overcome some simplifications made in the previous published studies to investigate such single-well systems in more detail and further resolve the governing physical processes. Focus of the study is on reservoirs with a low natural permeability (around 10^{-14} m^2). Firstly, an analytical solution is applied for justifying the numerical approach to produce consistent results for the presented simplest single-well design. Secondly, the efficiency of different single-well concepts is investigated via sensitivity analysis of variations in reservoir and operational parameters. Lastly, the previous study results are compared with the current approach for the gas-filled porous medium application. The results for the single-well system either with multi-laterals or without laterals demonstrate that the variation of permeability in different directions and the porosity play a crucial role on the overall performance. Single-well systems with multi-laterals are efficient, if the permeability is isotropic and in a range between 1×10^{-14} and $1 \times 10^{-12} \text{ m}^2$. The results of gas-filled pore space applications show that the capillary entry pressure has a significant impact on the wetting phase saturation. Simultaneous injection and extraction affect the saturation and heat exchange localized around the wells which decreases the thermal output power.

1. Introduction

A premise for the economic development of deep geothermal systems is that substantial reservoir volumes are accessed for long-term sustainable provision of thermal energy, while the cost for accessing the reservoir are kept low (Menberg et al., 2016; Ciriaco et al., 2020). Most attractive are amply explored, deep productive aquifers such as the Jurassic formations in the Paris Basin (Nader et al., 2016; Lopez et al., 2010) or the Southern German Molasse Basin (Birner et al., 2012), which host high volumes of hot groundwater that is extracted to supply heating facilities or power plants. The used groundwater is then injected back into the reservoir at sufficient distance to avoid thermal interference between extraction and injection wells (Banks, 2009). Such doublets, or more extraction and injection well combinations, are also the principle of Enhanced Geothermal Systems (EGS), which are considered for utilizing the gross of low-permeable deep formations (DiPippo, 2016). These projects rely on stimulation and artificial

fracture creation (Tester et al., 2006). Moreover, EGS are commonly designed as hot dry rock applications with circulation of artificial fluids (e.g. water, CO_2) due to the low accessible volume or absence of groundwater in deep, low-permeable formations (Brown, 2000; Pruess, 2006). In addition, the CO_2 -Plume Geothermal (CPG) heat extraction from naturally permeable formations has been proposed (Randolph and Saar, 2011; Garapati et al., 2015; Ezekiel et al., 2020). In this study, we also assume heat extraction from naturally permeable formations.

Currently, there exist several diverse concepts to guide the layout of extraction and injection wells. The traditional type is a doublet of deviated wells that start from a well pad near the geothermal plant and reach the reservoir at more than 1 km distance (Huenges, 2010). Also, it has been proposed to drill distinct horizontal wells in a deep formation with radial jet drilling (RJD) technology, with sufficient natural or engineered permeability of the reservoir between the well tracks (Blöcher, 2016; Nair et al., 2017; Bi et al., 2018). In multiple stage EGS, step-wise zonal fracturing is applied in the hot rock between these

* Corresponding author at: Petroleum and Natural Gas Engineering Department, Middle East Technical University (METU), Ankara, Turkey.

E-mail address: selerol@metu.edu.tr (S. Erol).

Nomenclature			
A	total area of the thermal source (m^2)	T_{in}	inlet temperature ($^{\circ}\text{C}$)
A_D	cooled area (m^2)	T_{out}	outlet temperature ($^{\circ}\text{C}$)
c	specific heat capacity ($\text{J kg}^{-1} \text{K}^{-1}$)	V	volume of the rock thermal source (m^3)
D	distance between injection and extraction laterals (m)	V_D	volume of the cooled zone (m^3)
D_{opt}	optimum distance between injection and extraction laterals (m)	v_T	thermal transport velocity (m s^{-1})
h	reservoir thickness (m)	u_{rad}	radial injection flow velocity (m s^{-1})
Q	heat flow rate (J s^{-1})	x, y, z	space coordinates (m)
Q	volumetric flow rate ($\text{m}^3 \text{s}^{-1}$)	<i>Greek symbols</i>	
\dot{m}	mass flow rate (kg s^{-1})	Θ	dimensionless temperature (i)
n	porosity (i)	β	thermal retardation factor (i)
P_t	thermal production term (W m^{-3})	κ	permeability (m^2)
P	pressure (Pa)	κ_r	relative permeability (i)
P_c	capillary pressure (Pa)	κ_{rw}	relative permeability of wetting phase (i)
P_{ov}	overpressure (Pa)	κ_{rnw}	relative permeability of non-wetting phase (i)
P_E	capillary entry pressure (Pa)	λ_m	bulk thermal conductivity of porous medium (W/m/K)
R	total radius of influence area of cooling (m)	ρ	density (kg/m^3)
R_w	flow front radius of the injected water (m)	σ	pore size distribution index (i)
R_T	temperature front radius of the injected water (m)	τ	dimensionless time (i)
r	radius vector (m)	φ_{out}	heat extraction flow rate (J s^{-1})
S_e	effective saturation (i)	<i>Subscripts</i>	
S_w	saturation of wetting phase (i)	<i>out</i>	outlet
S_{nw}	saturation of non-wetting phase (i)	<i>ov</i>	overpressure
S_{rw}	residual saturation of wetting phase (i)	<i>in</i>	inlet
S_{rnw}	residual saturation of non-wetting phase (i)	<i>m</i>	medium
t	time (s)	<i>p</i>	production
t_B	breakthrough time (s)	<i>r</i>	rock
t_L	operation time (s)	<i>w</i>	water
T	temperature ($^{\circ}\text{C}$)		
T_0	undisturbed reservoir temperature ($^{\circ}\text{C}$)		

horizontal wells (Li et al., 2016). As an alternative to the family of drillhole-based EGS, Zhao et al. (2020) discuss excavation based EGS that are using deep shafts to reach greater volumes of the deep hot dry rock than by drilling wells. Their argumentation is that roughly a hundred well pairs would be commonly needed to reach a full plant capacity of as high as 200 MW thermal energy. Another concept is that an integrated closed-loop lateral geothermal system at low depths ($< 1500 \text{ m}$) has been tested to avoid reservoir permeability issues (Toews, 2019). However, such closed-loop systems are strongly limited by slow conductive heat transfer through the pipes compared to open CPG and EGS systems.

As drilling costs are decisive for the realization of deep geothermal systems, the use of one single drill hole for extraction and injection is discussed (Wang et al., 2009; Nitschke et al., 2017; Huang et al., 2018; Song et al., 2017, 2018). Implementing one main wellbore that consists of concentric tubulars can reduce the overall drilling costs. Ideally, the main wellbore serves as backbone that feeds and receives the circulated fluid from well laterals at depth. The use of modern directional drilling techniques facilitates to perforate a great volume of the reservoir with multiple laterals to sustain a sufficiently high heat extraction rate. For instance, the layout by Peters et al. (2018) relies on multi-lateral wells leaving the backbone at 90° as small diameter radial laterals (radials, $< 5 \text{ cm}$) of up to 100 m length. Kant et al. (2018) present a technique, which locally increases the wellbore diameter by applying a thermal spallation process to the sidewalls of the borehole. This technique reduces the injection pressure during hydraulic stimulation which leads to optimized fracture propagation. Zhang et al. (2019a) proposes a tree-shaped layout with (sub)horizontal radials at different levels. This design is similar to that by Song et al. (2018), where the single-well principle is combined with the original multi-layer concept of parallel horizontal extraction and injection wells. Here, the heat

carrier water is injected in the upper formation and extracted from the lower formation through parallel sidetracked laterals.

The present study builds up on the numerical modelling study of Song et al. (2018) to further analyze the performance of the single-well multi-layer layout. The authors analyzed temperature and velocity fields of a synthetic single-well in a gas-filled porous medium and compared the heat extraction performances of four different well types. To enhance the water circulation between the horizontal injection and the extraction laterals (400 m vertical distance), some parallel slices which mimic fractures were included in the model. The results indicated that the output thermal power, extraction temperature, heat extraction ratio and accumulative thermal energy of this single-well are higher than those of conventional double vertical wells.

Song et al. (2018) employed some simplifications that are overcome in the present study. First, they implemented the laterals as simplified line sources and pipe flow dynamics are not accounted for. The presented approach enables to calculate only the pressure of single-phase flow leading to potential inconsistent estimations for gas-filled porous medium. A more reliable alternative to calculate the pressure of two phases (water and gas) filled porous media is to use a suitable capillary pressure function. Finally, Song et al. (2018) did not resolve the fluid flow in the single-well system from/to surface to/from the geological formation.

In a recent study, Shi et al. (2019) investigated the feasibility of single-well geothermal systems using supercritical CO_2 as a working fluid. Shi et al. (2019) segregated the numerical study into two parts; i) a three-dimensional (3-D) evaluation in the gas-filled porous medium identical to the reservoir model of Song et al. (2018); ii) addition of the pipe system from surface to the considered gas-filled porous medium (i.e., 0 m to 4 km). This second part was carried out with an advanced one-dimensional (1-D) pipe flow tool in COMSOL Multiphysics in which

the concentric tubulars can be taken into account. The results of their study demonstrate that the pressure decreases significantly from the formation to the surface (i.e., pressure drop > 15 MPa). The circulating CO₂ undergoes a phase change from liquid to air, which considerably reduces its bulk volumetric heat capacity, decreasing the thermal output power. However, the reservoir model of Shi et al. (2019) has the same limitations as the model of Song et al. (2018) as it relies on the same conceptual assumptions.

Our objective is to investigate such single-well systems in more detail and further resolve the governing physical processes. Therefore, the modelling approach of the current study builds up on the Brinkman and Navier-Stokes equations. Brinkman equations govern Darcy's law in the porous domains and the Navier-Stokes equations in the fast fluid flow regions represented by the laterals and the well system. The fluid flow is coupled with heat transport to account for non-isothermal flow dynamics. A 3-D numerical study is performed using COMSOL Multiphysics such as in the previous works by Shi et al. (2019) and Song et al. (2018) to assess the effect of multi-lateral wells on geothermal extraction and injection from a single-well. The efficiency of different single-well concepts is investigated via sensitivity analysis of variations in reservoir and operational parameters. In the following, first an analytical solution is applied for validation, and to adjust the spatial mesh and time steps of the numerical model. Among the many (semi-) analytical models available to evaluate thermal potential breakthrough between injection and extraction wells (e.g., Gringarten and Sauty, 1975; Lippmann and Tsang, 1980; Milnes and Perrochet, 2013; Wu et al., 2016; Zhang et al., 2019b), a combination of the most basic analytical solutions originally derived by Marx and Langenheim (1959) and Gringarten and Sauty (1975) and the solution of Zhang et al. (2019b) is utilized.

2. Methodology

2.1. Analytical model

Analytical solutions are crucial for validation of numerical models. The analytical solution introduced subsequently assumes a doublet geothermal system operating with constant water injection and extraction rates in/from a confined reservoir. It is customarily applied to estimate the downhole extraction temperature of a doublet system and the optimal well spacing between vertical wells, but it is equally suitable for representing two parallel horizontal laterals. The reservoir is simulated as homogeneous system with constant thickness, and the water flow follows Darcy's law. No heat and pressure losses along the wellbore depth are considered. The governing equation of the heat transfer in porous media in cylindrical coordinates is given as follows (Stauffer et al., 2013)

$$\rho_m c_m \frac{\partial T}{\partial t} = \lambda_m \frac{1}{r} \frac{\partial}{\partial r} \left(r \frac{\partial T}{\partial r} \right) - u \rho_w c_w \frac{\partial T}{\partial r} + P_t \quad (1)$$

in which u is the radial water flow velocity, r is the radial distance vector from the injection well, P_t is the thermal production term (heat production per unit volume and unit time), $\rho_m c_m$ is the volumetric heat capacity of the medium and λ_m is the bulk thermal conductivity.

The volumetric heat capacity is calculated as the weighted arithmetic mean of the rock $\rho_r c_r$ and volumetric heat capacity of water $\rho_w c_w$, considering the porosity n :

$$\rho_m c_m = (1 - n) \rho_r c_r + n \rho_w c_w \quad (2)$$

The bulk thermal conductivity is calculated as the geometric mean of the rock and water thermal conductivities:

$$\lambda_m = \lambda_w \lambda_r^{(1-n)} \quad (3)$$

The energy balance in a doublet well system is given as (Gringarten and Sauty, 1975)

$$V \rho_m c_m \frac{\partial T}{\partial t} = -\dot{m}_{out} c_w T + \dot{m}_{in} c_w T_{in} + Q \quad (4)$$

where V is the volume of the rock thermal source, T_{in} is the inlet water temperature, c_w is the heat capacity of the water, Q is the heat flow rate, \dot{m}_{out} and \dot{m}_{in} are the mass flow rates of the extraction and the injection wells, respectively. It is assumed that in the doublet well system injection and extraction mass flow rate can be identical, $\dot{m}_{out} = \dot{m}_{in}$.

The integration of the Eq. 4 yields the average temperature change in the reservoir:

$$T_0 - T = T_0 \left(1 - \exp \left(-\frac{\dot{m}_{out} c_w t}{V \rho_m c_m} \right) \right) - \frac{(\dot{m}_{in} c_w T_{in} + Q)}{\dot{m}_{out} c_w} \left(1 - \exp \left(-\frac{\dot{m}_{out} c_w t}{V \rho_m c_m} \right) \right) \quad (5)$$

where T_0 is the undisturbed reservoir temperature, Q is the heat flow rate defined by Marx and Langenheim (1959) as:

$$Q = \varphi_{out} \left(1 - \frac{G}{\psi} \right) \quad (6)$$

where the dimensionless parameters G and ψ are:

$$\psi = 4 \frac{(\lambda_r \rho_r c_r) t}{(\rho_m c_m)^2 h^2} \quad (7)$$

in which h is the reservoir thickness.

$$G = 2 \sqrt{\frac{\psi}{\pi}} - 1 + \exp(\psi) \operatorname{erfc}[\sqrt{\psi}] \quad (8)$$

The heat extraction flow rate from the extraction well is:

$$\varphi_{out} = \dot{m}_{out} c_w (T_{out} - T_{in}) \quad (9)$$

The volume of rock that is affected by a temperature change over time can be estimated based on the volume of the cooled zone. The ratio of the cooled area to the total area is proportional to the temperature decrease in the ground. Provided that the reservoir thickness is constant, the rate of change of the volume of the rock thermal source is estimated as:

$$V = V_D \frac{A}{A_D} \quad (10)$$

where V_D is the volume of the cooled zone, A is the total area of the thermal source (cross section of reservoir in x - z direction for horizontal laterals) and A_D is the cooled area (x - z direction), which changes over time and which is calculated as:

$$A_D = 2\pi R^2 + 2\pi RD \quad (11)$$

where D is the distance between injection and extraction wells, and R is the radius of influence of the cooling growing as the injection continues over time. R is estimated based on the heat advection including the water flow front (with radius R_w) and the temperature front of the injected water (with radius R_T). R_w can be calculated depending on the radial injection flow velocity as:

$$u_{rad}(r) = \frac{q_{in}}{2\pi hr} \quad (12)$$

$$R_w = u_{in}(r)t = \int_{r_b}^D \frac{q_{in}}{2\pi hr} t dr \quad (13)$$

where r_b is the well radius. The thermal transport velocity is given as:

$$v_T = \left(\frac{\partial r}{\partial t} \right)_T = -\frac{\rho_w c_w u_{rad}}{\rho_m c_m} \quad (14)$$

The ratio between hydraulic and thermal front effective velocities is the thermal retardation factor (de Marsily, 1986; Gossler et al., 2019) and given as:

$$\beta = \frac{u_{rad}}{v_T} = \frac{\rho_m c_m}{n \rho_w c_w} \quad (15)$$

The temperature front radius R_T can be calculated as the ratio between the velocity of the injection water temperature front and the thermal retardation factor β :

$$R_T = \frac{R_w}{\beta} \quad (16)$$

R_T presents the radii of the heat advection between injection and extraction wells. In addition, the heat conduction in cylindrical coordinates is included to estimate the radius of the area of influence due to injection. The equation for horizontal conductive heat transport in cylindrical coordinates is given as:

$$u_{rad} \rho_w c_w \frac{\partial T}{\partial r} = \lambda_m \frac{1}{r} \frac{\partial}{\partial r} \left(r \frac{\partial T}{\partial r} \right) \quad (17)$$

By integrating Eq. 17 twice on both sides (Zhang et al., 2019b), T is defined as:

$$T = C_1 \frac{\lambda_m}{\rho_w c_w} \frac{2\pi h}{q_{in}} r \left(\frac{\rho_w c_w}{\lambda_m} \frac{q_{in}}{2\pi h} - 1 \right) + C_2 \quad (18)$$

whereas q_{in} is the volumetric flow rate at the inlet, C_1 and C_2 are the integral constants. The boundary conditions are defined as $r = r_b$, $T = T_{in}$; $r = R_T$, $T = T_{in}$ to determine the integral constants as:

$$\left. \frac{\partial T}{\partial r} \right|_{r=R_T} = C_1 \frac{\lambda_m}{\rho_w c_w} \frac{2\pi h}{q_{in}} r \left(\frac{\rho_w c_w}{\lambda_m} \frac{q_{in}}{2\pi h} - 1 \right) \quad (19)$$

After determining the integral constants, the radius of the influence area is calculated as:

$$R = \left[\frac{(T_0 - T_{in})}{10^{-6}} R_T \left(\frac{\rho_w c_w}{\lambda_m} \frac{q_{in}}{2\pi h} - 1 \right) \right] \left(\frac{\lambda_m}{\rho_w c_w} \frac{2\pi h}{q_{in}} \right) \quad (20)$$

Finally, the radius of the cooling area growing over time, R_c , can be inserted into Eq. 11 to estimate the rate of change in the volume of the rock thermal source (Eq. 10).

The combination of Eq. 5 to 10 provides an approach to estimate the temperature change at any radial distance from the injection well. The temperature change occurring at the extraction well can be calculated as:

$$T_{out} = T_0 - \frac{G(T_0 - T_{in})(\rho_m c_m)^2 h^2}{4(\lambda_r \rho_r c_r) t} \left(1 - \exp \left(-\frac{\rho_w c_w q_{in} t}{V \rho_m c_m} \right) \right) \quad (21)$$

In dimensionless form, the temperature change is given as:

$$\Theta_p = \frac{\varpi G}{4\tau} \left(1 - \exp \left(-\tau \frac{D^2 h}{V} \right) \right) \quad (22)$$

where the dimensionless temperature $\Theta_p = T_{out} - T_0 / T_0 - T_{in}$, the other dimensionless parameters τ and ω are:

$$\varpi = \frac{\rho_w c_w \rho_m c_m q_{in} h}{\lambda_r \rho_r c_r D^2} \quad (23)$$

$$\tau = \frac{\rho_w c_w q_{in} t}{\rho_m c_m D^2 h} \quad (24)$$

The breakthrough time which is the time needed for the thermal front after starting the operation of a double well system to reach the extraction well, can be estimated according to Lippmann and Tsang (1980)

$$t_B = \frac{\pi n h D^2}{3 q_{in}} \beta \quad (25)$$

The optimal well spacing between injection and extraction wells is given by Gringarten and Sauty (1975) as:

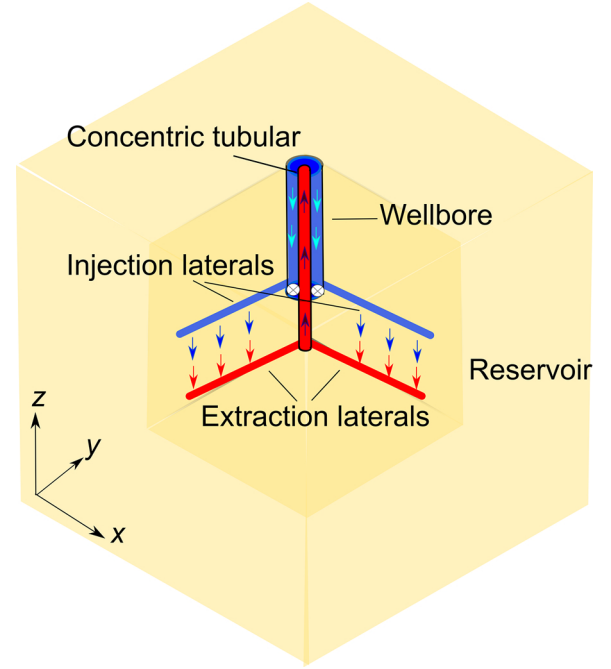


Fig. 1. Illustration of a single-well multi-layer concept examined by this numerical modelling study.

$$D_{opt} = \left[\frac{2q_{in} t_L}{\left(\beta h + \left(\beta^2 h^2 + 2 \frac{\lambda_r \rho_r c_r}{(\rho_w c_w)^2} t_L \right)^{1/2} \right)} \right]^{1/2} \quad (26)$$

where t_L is the total operation time considered for the doublet. Eq. 26 facilitates to determine an appropriate distance between upper and lower laterals in the vertical direction.

2.2. Numerical model setup

To evaluate in detail the performance of a single-well system with multi-lateral drills (Fig. 1), a numerical model domain is divided into two sub-domains. The first sub-domain represents the reservoir layer. It is represented by a three-dimensional (3-D) reservoir model in which injection and extraction take place (the depth range is from 4 km to 4.3 km). The second sub-domain represents the medium from the reservoir to the surface and is modelled as a two-dimensional (2-D) axisymmetric model, where the heat transfer takes place over a long distance along the well (the depth range is 0 m to 4 km). The water flow velocity, pressure and the temperature calculated in the first sub-domain are used as the boundary conditions for the 2-D model. The numerical study is performed using the finite element program COMSOL Multiphysics (version 5.4). Several features of COMSOL Multiphysics are selected to model the two sub-domains, in particular the “Free and porous media” feature in the subsurface module is coupled with the heat transfer module.

In the first sub-domain, the single-well is positioned at the center of the domain (Fig. 2). The extension of the model in x and y directions is equal at 1000 m, and it is 600 m in z direction. The reservoir thickness is 300 m, and it assumed to be a water-saturated porous medium. At the bottom of the model an impermeable solid rock layer is assumed, where the heat transfer is driven only by conduction. The impact of the permeability of this solid rock layer has been tested and results revealed that permeability lower than $1 \times 10^{-18} \text{ m}^2$ beneath the reservoir has a negligible impact on the heat extraction. The length of the laterals is fixed to 100 m and the inner diameter to 10 cm. The water injection and extraction laterals are considered as screened horizontal wells, whereas

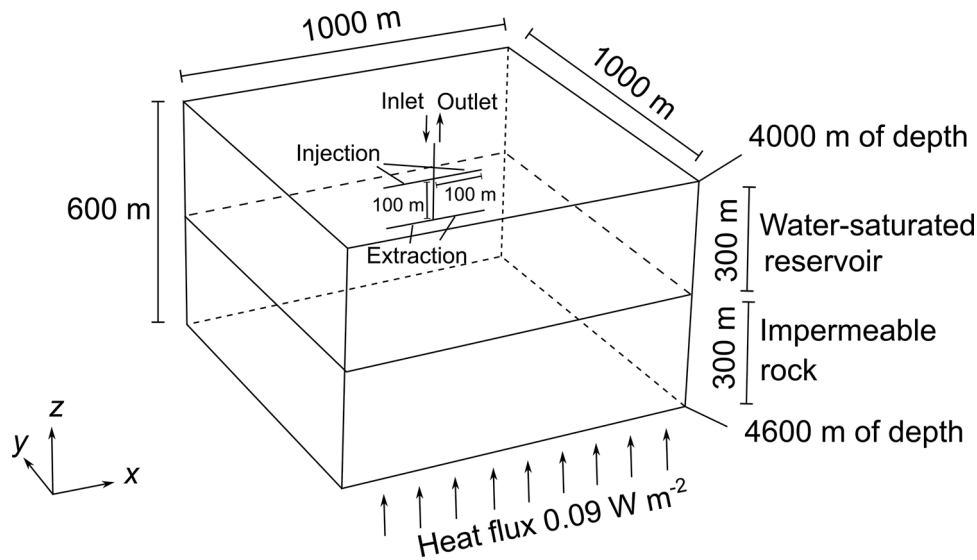


Fig. 2. 3-D numerical model for single-well with multi-laterals (first sub-domain). Inlet represents the source, and outlet denotes the sink.

the vertical portion of the well has interior walls (no-slip BC) from surface to the depth of the sidetracked laterals. The water is injected into the reservoir laterals which are at the top, and the extraction laterals are located 100 m below. The optimal distance between upper and lower laterals is determined using Eq. 26. This distance ranges from 60 m to 100 m depending on the flow rate injected from a single lateral (i.e., 7.5 to 15 kg s⁻¹). The 3-D model consists of 3.7–7 million elements depending on the configuration of the system (i.e., number of laterals). The mesh is generated using tetrahedral elements. Moreover, the mesh is refined by using the corner refinement and boundary layer tools in the software. Further details on the meshing are given in Table 1. The number of generated elements for the models and runtimes can be found in Appendix A.

To generate the initial state, the thermal gradient is assigned to be 0.03 K m⁻¹, while the surface temperature is 12 °C. The simulation time is set to 30 years of continuous production. The confining pressure increases with a pressure gradient of 1 × 10⁴ Pa m⁻¹.

In the first sub-domain (i.e., 3-D model), one of the most challenging parts is to choose a realistic boundary condition for a single-well geothermal system, which is essential to produce meaningful results. Closed (Dirichlet type) and open (Cauchy type) boundary conditions are examined regarding to all aspects of model setup (e.g., production temperature, injection flow velocity). As a consequence, to evaluate the straight impact of fluid flow due to the short distance between the injection and extraction laterals, closed boundary conditions are applied at the side walls of the model for flow and heat transport. The source (injection) is specified as fixed mass flow rate and fixed injection temperature. The sink (extraction) is defined as fixed pressure. At the bottom of the model, the heat flux is fixed to 0.09 W m⁻² ($\lambda_m \times T_{grad} = 3 \text{ W m}^{-1} \text{ K}^{-1} \times 0.03 \text{ K m}^{-1}$).

The water flow field is firstly calculated in steady-state conditions via the Brinkman equation which governs the Navier-Stokes equations in the fast water flow in the lateral channels, and via Darcy's law in the porous domain. The water flow is coupled with heat transfer for non-isothermal flow. In order to improve the convergence of the computational fluid dynamic (CFD) calculations, a ramping parameter

multiplied with the water dynamic viscosity parameter is applied. In the stationary study step, an auxiliary sweep of ramping parameters for values of 1000, 100, 10, and 1 is used. The auxiliary sweep finds a solution for the first value and uses this solution as the initial condition for solving the next value. The sweep continues in a way until the ramping parameter reaches a value of 1, that is, the problem is solved for the actual water dynamic viscosity. The stationary solution is used in this step to achieve convergence of the coupled water flow and the heat transfer calculations. In the second step, the heat transfer coupled with the non-isothermal water flow over time is calculated. For this, the non-linear iterative solver type Generalized Minimal Residual method (GMRES) is used both for steady-state laminar flow and for time dependent coupled heat transfer calculations. The Backward Euler (Crank-Nicolson scheme) time marching method is applied as numerical solver with relative error tolerance of 10⁻³, which is the default value and typically controlled by the simulator. In a sensitivity analysis it was found that a lower error tolerance of 10⁻⁶ has no crucial impact on the simulated outlet temperature. Thus, we adapted an error tolerance of 10⁻³ to avoid larger computational effort. The second sub-domain represents the water flow in the 0.4 m diameter well and the heat exchange along the vertical part of the well (between the well and the surrounding ground from the reservoir to the surface). The temperature of the extracted water, pressure and flow conditions at the outlet pipe obtained from the calculations in the first sub-domain (at the top of the reservoir) are implemented as boundary conditions into the second sub-domain 2-D axisymmetric model (at the bottom of the extraction tube at 4 km). The radius of the inner extraction tube is 0.1 m. The insulation thickness between the injection and extraction tubes is set to 0.03 m. The cross section of the outer injection pipe is 0.0726 m², whereas the inner extraction pipe has a cross-section of 0.0314 m². Therefore, the flow velocity in the injection pipe is slower compared to the one in the extraction pipe, which enhances the heat exchange from surface to the reservoir between the injected water and the surrounding formations. The initial and boundary conditions of the second sub-domain are identical to the first sub-domain model.

The mesh consists of triangular elements and the model domain

Table 1

Optimum element sizes and meshing parameters for the first sub-domain (3-D reservoir model).

Elements	Max. element size (m)	Min. element size (m)	Max. element growth rate	Curvature factor	Resolution of narrow regions
For general model	17.5	0.5	1.35	0.3	0.85
For fluid dynamics	7.9	0.4	1.08	0.3	0.95

consist of approximately 2.2 million of elements. The mesh characteristics are given in Table 2. For CFD calculations and coupled heat transfer, numerical methods and strategies are identical to the ones applied in the first sub-domain (Fig. 3).

Thermal and hydraulic properties of porous medium used for the validation of the basic numerical model is given in Table 3. Other parameters of the modelled porous media for further analyses are extensively provided in Table 5.

2.3. Validation of numerical model

In this section the results of the developed numerical model are compared with the results obtained using the analytical approach described before. The objective of the comparison is to ensure that the numerical approach is able to produce realistic and accurate results for the simplest single-well design presented in Fig. 2. This step ideally enables to demonstrate that the mesh refinement and time steps optimization approach proposed in the previous section is valid.

The 3-D numerical model results obtained at the extremity of the extraction lateral can be compared with the downhole extraction temperature calculated using Eq. 21. The assumptions that need to be made for the analytical calculation are a radial distance of 100 m away from the injection point and a depth of 4 km. When applying such parameters, the numerical results fairly agree with the analytical approach results for both the extraction temperature and the dimensionless downhole temperature over time (Fig. 4). This agreement suggests that the numerical approach (model definition, equations used, and numerical parameters chosen) is able to provide accurate results when it comes to modelling complex geometries of single-well systems, for example, with variable numbers and locations of laterals.

2.4. Scenarios examined for efficiency analysis

In the following, we use the numerical model developed in this study to inspect the impact of radial lateral configuration, injection flow rate, injection water temperature and reservoir permeability on the efficiency of the single-well system. The insight obtained from the scenarios inspected serves to determine the optimal injection and extraction parameters for sustainable system application. In addition, the single-well multi-lateral layouts are tested in two cases to justify the effect of anisotropic and isotropic permeability. Although, the anisotropic permeability in the nature can be found mostly larger in x and y direction and lower in z direction, we set the values vice versa to examine the interference between lateral configurations.

We refer to a single-well multi-lateral layout as base case, and all scenarios are compared to this reference as described in Table 4. The density of water is calculated in COMSOL as a function of temperature and pressure with the coupled “*Multiphysics*” component. Since the dynamic viscosity of water is used as a ramping parameter, an empirical equation of the dynamic viscosity of water derived by Likhachev (2003) is implemented into the model. This solution has a temperature range of 273 – 573 K and a pressure range of 0.1 – 80 MPa. The salinity of water is ignored.

First, the impact of different lateral configurations on heat production is evaluated. The examined well arrangements are three layouts of laterals and one configuration without. For all configurations, the injection takes place at 4.1 km of depth, and extraction is at 4.2 km.

The simplest “no laterals” scenario representing a wellbore without

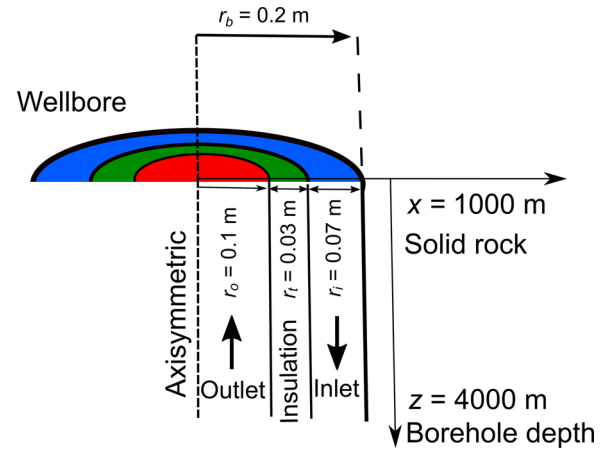


Fig. 3. 2-D axisymmetric model for concentric tubular system (second sub-domain).

Table 3

Thermal and hydraulic parameters of both sub-domains for the validation of the numerical model.

Parameter	Value
Porosity	0.05
Isotropic reservoir permeability	$1 \times 10^{-14} \text{ m}^2$
Bulk thermal conductivity of porous medium ^a	$3 \text{ W m}^{-1} \text{ K}^{-1}$
Bulk volumetric heat capacity of porous medium ^b	$3 \text{ MJ m}^{-3} \text{ K}^{-1}$

^{a,b} Calculated with Eq. 3 and Eq. 2, respectively.

laterals is depicted in Fig. 5a. For the configuration “2 = 2” in Fig. 5b, we assume two injection laterals in the upper part of the reservoir and two extraction laterals in the lower part of the reservoir (2 = 2 laterals arrangement). The 4 = 4 lateral configuration can be seen in Fig. 5d. As default, the upper injection lateral wells are parallel to the lower extraction lateral wells and the angle between the lateral wells and the wellbore is 90°. In configuration 2 × 2 shown in Fig. 5c, this is modified: the upper and lower elements are staggered, realized by a 90° horizontal rotation of the injection lateral wells with respect to the extraction laterals.

2.4.1. Scenarios

The 2 = 2 parallel lateral configuration (Fig. 5b) is determined as the reference configuration, and the heat extraction performance is compared with different scenarios based on the impact of mass flow rate, role of injection water temperature and effect of reservoir permeability. Scenarios with specific variants are listed in Table 5. In each scenario, one variant is set as the base case (Table 4), and the rest of the initial and boundary conditions are identical for three scenarios.

Scenario 1 is considered to determine the impact of variable mass flow rate on the performance of a system. The mass flow rate is typically adjusted with respect to the heat demand.

The aim of Scenario 2 is to evaluate the influence of the returning water temperature on the thermal output power. The injection water temperature drives the life-time of a geothermal system. The returning water temperature is based on the functioning of the heat exchanger, separator or the heat pump on the surface. Most of the doublet geothermal systems in Europe are operated with returning fluid

Table 2

Optimum element sizes and meshing parameters for the second sub-domain, the 2-D axisymmetric wellbore model.

Elements	Max. element size (m)	Min. element size (m)	Max. element growth rate	Curvature factor	Resolution of narrow regions
For general model	268	1.2	1.3	0.3	1
For fluid dynamics	45	0.4	1.15	0.3	0.95

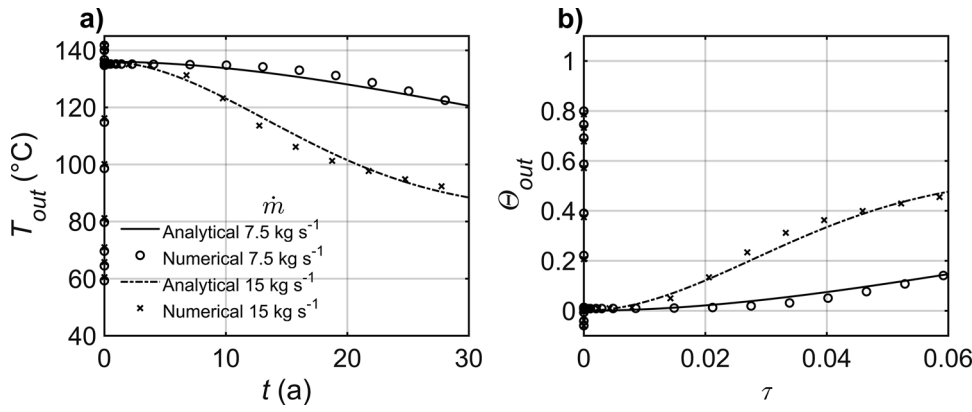


Fig. 4. Validation of numerical model: a) extraction temperature over time; b) temperature versus time in dimensionless form. Θ_p is the dimensionless temperature (Eq. 22), τ is the dimensionless time (Eq. 24). RMSE between analytical and numerical solution is 0.54 °C for $\dot{m} = 7.5 \text{ kg s}^{-1}$, and RMSE = 1.74 °C for $\dot{m} = 15 \text{ kg s}^{-1}$. Isotropic permeability $1 \times 10^{-14} \text{ m}^2$.

Table 4
Characteristics and thermal properties of base case model.

Parameters	Value
Bulk thermal conductivity of porous medium ^a	3 W m ⁻¹ K ⁻¹
Bulk volumetric heat capacity of porous medium ^b	3 MJ m ⁻³ K ⁻¹
Thermal conductivity of insulation	0.04 W m ⁻¹ K ⁻¹
Injection temperature	40 °C
Thermal gradient	0.03 K m ⁻¹
Surface temperature	12 °C
Reservoir temperature at 4000 m of depth	140 °C
Pressure gradient	1 × 10 ⁴ Pa m ⁻¹
Injection mass flow rate	30 kg s ⁻¹
Case 1 – isotropic reservoir permeability	1 × 10 ⁻¹⁴ m ²
Case 2 – anisotropic reservoir permeability	κ_x and $\kappa_y = 1 \times 10^{-15} \text{ m}^2$, $\kappa_z = 1 \times 10^{-14} \text{ m}^2$
Porosity	0.05
Vertical spacing between injection and extraction laterals	100 m
Lateral radius	0.05 m
Lateral length	100 m
Wellbore radius	0.2 m
Wellbore outlet pipe radius (inner part of the wellbore)	0.1 m
Wellbore insulation thickness	0.03 m
Wellbore inlet pipe radius (outer part of the wellbore)	0.07 m (cross section 0.0314 m ²)

^{a,b}Calculated with Eq. 3 and Eq. 2, respectively. Wellbore concentric tubular scheme is given in Fig. 3. Dynamic viscosity of water and the density are calculated as a function of temperature and pressure.

Table 5
Parameters of scenarios with their specific focus and parametric variants.

Scenario	Variants	Injection temperature (°C)	Mass flow rate (kg s ⁻¹)	Isotropic reservoir permeability (m ²)
Scenario 1 (impact of mass flow rate)	1	40	15	1 × 10 ⁻¹⁴
	2 (base case)		30	
	3		60	
Scenario 2 (role of injection water temperature)	1	30	30	1 × 10 ⁻¹⁴
	2 (base case)	40		
	3	60		
Scenario 3 (effect of reservoir permeability)	1	40	30	1 × 10 ⁻¹³
	2 (base case)			1 × 10 ⁻¹⁴
	3			1 × 10 ⁻¹⁵

temperatures of 30 °C to 60 °C to sustain their performance over decades, and the thermal interference between injection and extraction wells is avoided with appropriate distance of the boreholes. In a single-well concept, it is likely that the distance between injection and

extraction wells is short to interfere, and the cold plume of injected water from the injection well reaching the extraction well can cause thermal breakthrough early. The distance as well as the temperature range for injection thus have an impact on the sustainable performance of the system.

The objective of Scenario 3 is to evaluate the impact of the reservoir permeability (isotropic) both on the production performance and the injection pressure. Permeability of a reservoir in geothermal fields has a major influence on both productivity and the sustainability of fluid circulation (Eggertsson et al., 2018). In particular for a single-well system, permeability is more important due to the short distance between injection and extraction wells. If the permeability is high, the injected fluid may quickly reach extraction well which lowers the extraction temperature. If the permeability is very low, then the production may stop if the required high injection pressure is not accomplished.

2.5. Comparison with previous study

In addition to the application of the methodology in water-filled porous medium, the numerical approach is applied to gas-filled porous medium. The numerical results obtained are compared to those obtained by Song et al. (2018) with their COMSOL implementation. Song et al. (2018) calculated flow velocity applying the Darcy's law single phase tool in a gas-filled porous medium. They considered the lateral wells as 1-D line sources. In their approach, the extraction temperature is evaluated based on an integration method over the line sources (lateral wells) and given as follows

$$T_p = \frac{\int_L T(t) dl}{L} \quad (27)$$

In contrast to the methodology of Song et al. (2018), the Phase Transport in Porous Media tool is coupled with the Darcy's law tool in this current study. The phase transport module in COMSOL Multiphysics to couple gas and water flow is suited for simulating injection into gas-filled porous medium. The Phase Transport in Porous Media tool computes the flow velocity and pressures of both gas and water phases, using a capillary pressure function.

Two widely used approaches exist in COMSOL Multiphysics to calculate the capillary pressure which are after Brooks and Corey (1966) and van Genuchten (1980). The Brooks and Corey (1966) approach comprises two fitting parameters to represent the pore size distribution index and entry capillary pressure. The approach is given as

$$P_c = P_{Ee} S_e^{-1/\sigma} \quad (28)$$

$$\kappa_{rw} = S_e^{(3+2/\sigma)}, \quad \kappa_{rnw} = (1 - S_e)^2 (1 - S_e^{(1+2/\sigma)}) \quad (29)$$

in which κ_{rw} and κ_{rnw} are the relative permeability of wetting and non-wetting phases, respectively. P_E is entry capillary pressure, which is the pressure required by the wetting phase to displace the non-wetting

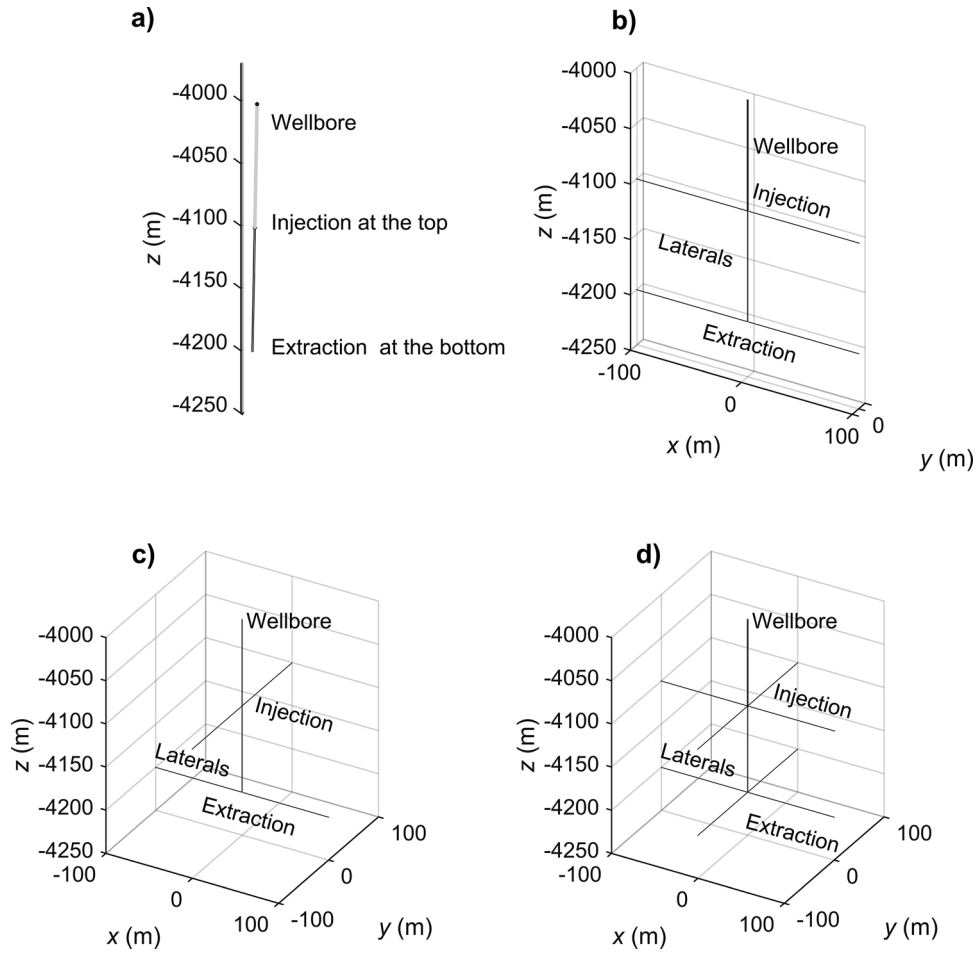


Fig. 5. Illustration of a single-well with various lateral configurations: a) without laterals; b) Base case layout 2 = 2 with parallel radial laterals (two injection, two extraction); c) layout 2 + 2 with two injection laterals rotated by 90°; d) layout 4 = 4 with parallel radial laterals.

phase in pore system. In our case, the wetting phase is water and the non-wetting phase is gas. S_e is the effective saturation calculated as follows

$$S_e = \frac{S_w - S_{wr}}{1 - S_{wr} - S_{nr}} \quad (30)$$

where S_w and S_{nw} are the saturation of wetting and non-wetting phases scaled by residual wetting and non-wetting saturations S_{rw} and S_{rnw} .

The [van Genuchten \(1980\)](#) approach for capillary pressure and relative permeabilities of wetting and non-wetting phases are given as

$$P_c = P_E (S_e^{-1/m_G} - 1)^{(1-m_G)} \quad (31)$$

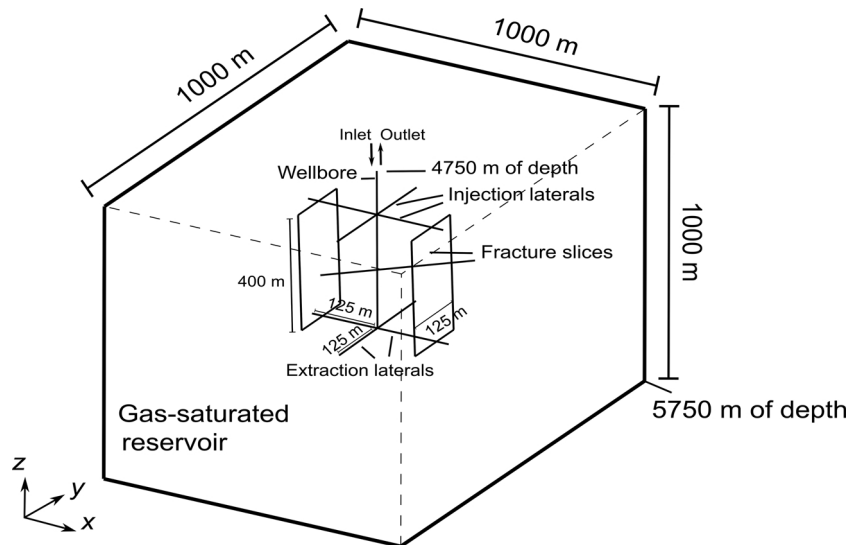


Fig. 6. Illustration of single well model identical to that by [Song et al. \(2018\)](#).

$$\kappa_{rw} = S_e^{l_G} [1 - (1 - S_e^{1/m_G})^{m_G}]^2, \kappa_{rmw} = (1 - S_e)^{l_G} (1 - S_e^{1/m_G})^{2m_G} \quad (32)$$

where l_G and m_G are the constitutive relation constants.

The main difference between these two capillary pressure approaches is that the Brooks and Corey equation provides a smoother prediction in the saturation front with rising capillary pressure compared to the van Genuchten equation (Büsing et al., 2014). For this reason, the Brooks and Corey approach is typically used to evaluate the capillary pressure and relative permeability.

The entry capillary pressure is crucial to displace the non-wetting phase (gas) to wetting phase (injected water). Theoretical methods to predict the capillary entry pressure value are typically ad hoc and often based on the pore throat radius and the interfacial tension between the non-wetting and wetting phases. Revil et al. (1998) estimated the entry capillary pressure based on the average grain diameter and pore throat for different granular porous media. According to their study, grain diameters of 300 μm , 100 μm and 7 μm yield entry capillary pressures of 3 MPa, 10 MPa and 144 MPa, respectively.

In order to inspect the impact of the entry capillary pressure on the saturation degree of the wetting phase, we have tested the gas-filled porous medium application in the revised manuscript with two different capillary entry pressure values. For the first one, the entry capillary pressure is set to 1 MPa, and to 10 MPa in the second application. In both of the application models, the pore size distribution index is set to 3 (Assouline, 2005).

Fractures are set as slices between injection and extraction laterals similar to Song et al. (2018) (Fig. 6).

The water flow in the fracture slices is calculated via Darcy's law and the boundary of fracture slices are driven by the pressure solved via Brinkman equations. The parameters set in the numerical model are identical to those by Song et al. (2018) and given in Table 6.

3. Results

3.1. Configuration of laterals

The heat extraction performance is examined comparing four types of single-well configurations tested with isotropic and anisotropic permeability cases. Figs. 7 and 8 demonstrate anisotropic and isotropic cases, respectively and depict the extraction temperature and the thermal outlet power at the surface over time (i.e., at 0 m). Runtimes of the simulations and the number of generated elements for the models can be found in Appendix A.

The impact of anisotropy in the permeability on the heat extraction is larger than the lateral well arrangements. It is expected that the radial flow through the laterals distributes the injected mass flux of water along the laterals and thus enhances the heat transfer per rock volume. An anisotropic permeability affects the radial flow velocity towards the extraction laterals. Fig. 7a reveals that in a reservoir with anisotropic permeability the single-well 2 + 2 configuration has the longest breakthrough time and the 2 = 2 configuration has the shortest. In contrast, in the isotropic case the single-well without laterals has the shortest breakthrough time and the 4 = 4 configuration has the longest (Fig. 8a). In the anisotropic case, lower permeability values in x and y direction and larger in z direction cause faster water flow between laterals if the layout configurations are aligned (i.e., layouts 2 = 2 and 4 = 4). As depicted in Figs. 7b and 8b, the 2 + 2 configuration is favorable in the anisotropic case due to the considerably longer flow path towards extraction laterals, whereas 4 = 4 layout is more efficient in a reservoir with isotropic permeability. The latter is caused by subdividing the total injection rate into four laterals, which yields a lower water flow velocity in the porous medium.

Table 7 shows the water flow velocity and the injection pressure of different lateral layouts. For the single-well without laterals, the overpressure is more than 12 MPa without laterals, whereas the water injection pressure for the other layouts with laterals is in a range

2–6 MPa. The reason for this difference can be found in the contact area of water injection. The tube directly injecting into the porous domain without laterals has a contact surface area of 0.0726 m^2 . In comparison, a long lateral offers a considerably larger cylindric contact area for injection ($\sim 31.4 \text{ m}^2$). The 2 = 2 and 2 + 2 lateral configurations have 62.8 m^2 of surface area for injection, while the 4 = 4 layout has 125.6 m^2 . Therefore, the required force applied per surface area to push the water through porous media is reduced with the laterals.

The impact of the concentric tubular on the temperature obtained with the 2-D axisymmetric model is illustrated in Fig. 9 (second sub-domain). The injected water temperature increases from the surface to the reservoir by approximately 7 $^\circ\text{C}$ to 5 $^\circ\text{C}$ over 30 years. For instance, when the water injection temperature is fixed to 40 $^\circ\text{C}$ at the inlet, the water in the injection tube at 4 km of depth reaches 45 $^\circ\text{C}$ (flow injection surface area along the depth is $\sim 5024 \text{ m}^2$). A larger surface contact area of the injection tube slightly enhances the heat transfer with the surrounding ground along the depth due to the associated slower water flow velocity. The extraction water temperature drops by around 3 $^\circ\text{C}$ to 2 $^\circ\text{C}$ from the reservoir depth to the surface (extraction flow cross section area is 0.0314 m^2). This demonstrates that the smaller cross section area for the extraction tube provides an advantage to decrease the heat loss from reservoir to surface. As the inlet temperature on the return pipe is raised, the temperature difference from the reservoir to surface is smaller. As the temperature quickly reaches steady state conditions in the concentric tubular system, the insulation thickness has minor impact on the injected and extracted water temperature due to lower thermal conductivity of insulation (0.04 $\text{W m}^{-1} \text{K}^{-1}$).

3.2. Impact of mass flow rate

Overall performance of three variants significantly varies based on the mass flow rate, \dot{m} (Fig. 10). The outlet temperature with the highest mass flow rate (variant 3) dramatically decreases, but the thermal output is superior compared to the other variants. In addition, the required pressure of variant 3 for the injection is nearly twice that of variant 2 (Table 8). The lower mass flow rate of variant 1 provides sustainable thermal output over time but only produces 5 to 4 MW of thermal heat over 30 years of operation.

3.3. Role of water injection temperature

Fig. 11 reveals that the outlet temperature drop is proportional to the injection temperature. The magnitude of the thermal output power increases as the injection temperature declines. The injection water temperature has secondary importance on the performance of the system operation and is proportional to the demand on heat produced.

Table 6

Equivalent numerical model parameters in Song et al. (2018) and the current study.

Parameters	Value
Bulk thermal conductivity of reservoir	2.8 $\text{W m}^{-1} \text{K}^{-1}$
Bulk volumetric heat capacity of reservoir	2.952 $\text{MJ m}^{-3} \text{K}^{-1}$
Injection temperature	40 $^\circ\text{C}$
Undisturbed reservoir temperature at the top boundary	220 $^\circ\text{C}$
Thermal gradient	0.04 K m^{-1}
Injection mass flow rate	30 kg s^{-1}
Matrix permeability	1 $\times 10^{-15} \text{ m}^2$
Matrix porosity	0.15
Fracture aperture	0.001 m
Isotropic fracture permeability	1 $\times 10^{-11} \text{ m}^2$
Fracture porosity (vuggy pores included)	0.15
Fracture width	125 m
Fracture length	400 m
Fracture horizontal well spacing	75 m
Distance between injection and extraction laterals	400 m

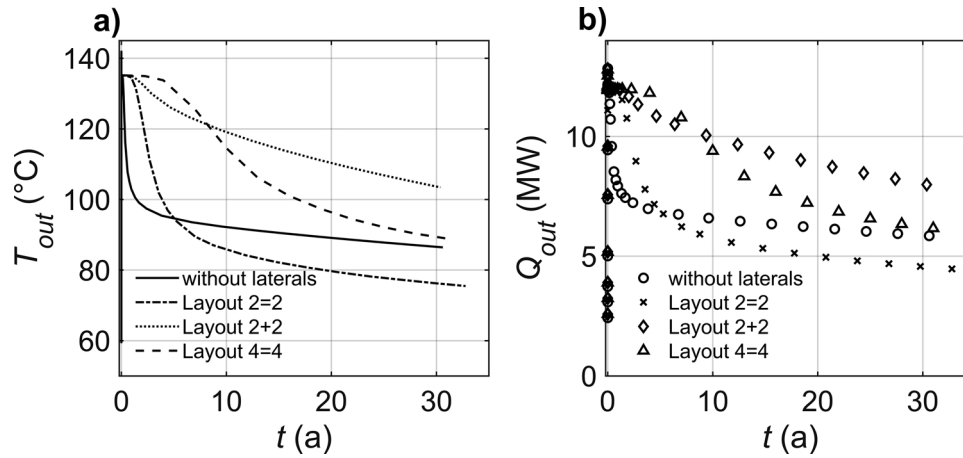


Fig. 7. Performance comparison of different single-well configurations for the anisotropic permeability case 1 (κ_x and $\kappa_y = 1 \times 10^{-15} \text{ m}^2$, $\kappa_z = 1 \times 10^{-14} \text{ m}^2$). Table 4 lists the model parameters.

3.4. Effect of reservoir permeability

Overpressure is evaluated as a function of isotropic reservoir permeability with the 2 = 2 lateral well layout depicted in Fig. 5b. The overpressure increases exponentially as the permeability decreases (Fig. 12b). The overpressure management for reducing the risk to trigger seismicity is important for injection (Nicholson and Wesson, 1990). It can be seen that an isotropic permeability value under $1 \times 10^{-14} \text{ m}^2$ causes larger overpressure in the order of 30 MPa. The numerical model does not take into account the shear stress of the rock. However, fluid injection within overpressure ranges of lower than 10 MPa, particularly in sedimentary rocks, do not usually induce seismicity greater than a magnitude of $M_1 = 2$ (Evans et al., 2012). Injection operations in low permeability ($< 5 \times 10^{-15} \text{ m}^2$) formations can exceed the maximum sustainable injection pressure. This has the potential of triggering sensible earthquakes on critically stressed faults (Villarrasa and Carrera, 2015).

In addition to overpressure management, existing natural fractures or faults for a single-well configuration can either provide improvement for the water circulation through porous media and thus volume accessed for heat exchange, or it can cause a short-circuit for the flow, particularly in gas-filled pores may push the water for shorter paths due to capillary pressure. In the following section, thus the impact of gas-filled pores is tested in more detail.

According to Adams et al. (2015), CPG systems that use supercritical/gaseous CO_2 provide more electric power than systems using

water or brine as working fluid in a reservoir with isotropic permeability between $1 \times 10^{-13} \text{ m}^2$ and $1 \times 10^{-14} \text{ m}^2$. In contrast, identical systems have higher production efficiency when using water or brine when the permeability is between $1 \times 10^{-12} \text{ m}^2$ and $1 \times 10^{-13} \text{ m}^2$. Based on the findings of Adams et al. (2015), the use of supercritical/gaseous CO_2 is more favorable in a reservoir with lower permeability ($< 1 \times 10^{-13} \text{ m}^2$) due to its lower dynamic viscosity and density requiring less injection pressure compared to that of water.

3.5. Comparison with previous study

Fig. 13 depicts a comparison of our results with those of the previous study by Song et al. (2018) over an operation period of 30 years. The current study simulations are performed using two different representations of the capillary entry pressure. The calculated thermal output power of the current study is simply multiplied with the wetting saturation (i.e., injected water) ratio near the extraction well. The steam is neglected.

In the current study, applying the two-phase flow models for gas-saturated reservoir yields a sharp decline of the outlet temperature by approximately 40 % after a couple of days with both of the capillary entry pressure values, whereas the temperature drops only by 2.5 % in the model by Song et al. (2018). In addition, the extracted thermal power given by Song et al. (2018) is considerably larger. It is likely that in their study they assumed that the reservoir was already filled with the injected water and the extraction has started after a while. The

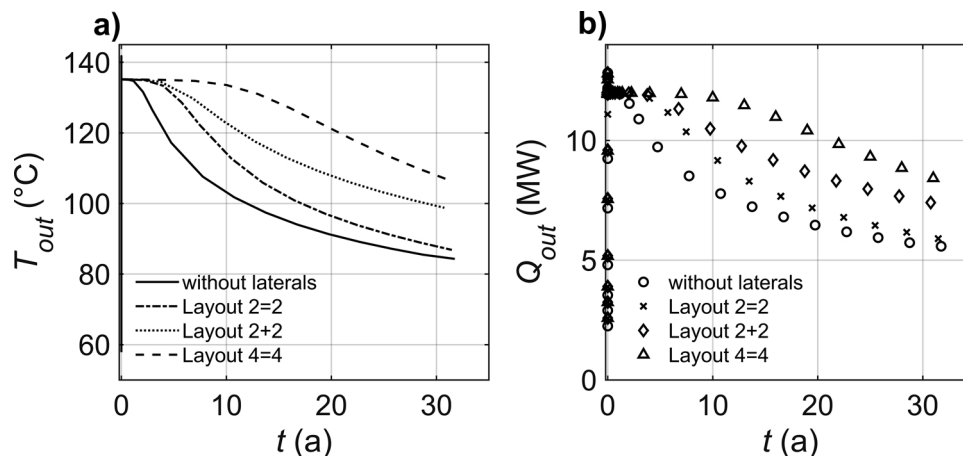
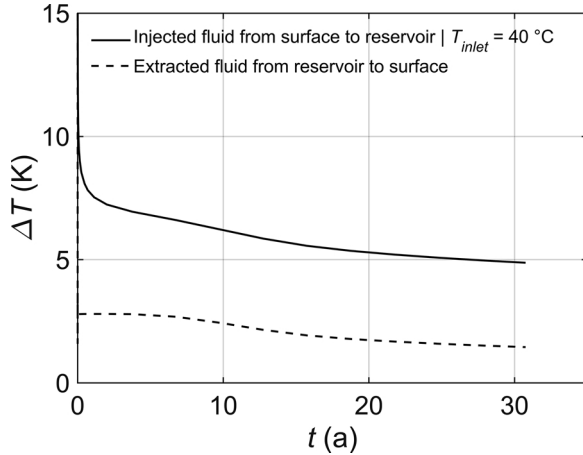


Fig. 8. Performance comparison of different single-well configurations for the isotropic permeability case 2 ($\kappa = 1 \times 10^{-14} \text{ m}^2$). The model parameters can be found in Table 4.

Table 7

Comparison of flow velocity and injection pressure results of lateral configurations.

Configuration	Average water flow velocity (kg s ⁻¹)	Maximum water flow velocity (m s ⁻¹)	Overpressure at 4 km of depth (MPa) ^b	Total injection contact surface area (m ²)
Single-well without laterals	0.38	0.89	12	0.0726
Layout 2 = 2	1.38 ^a	4.02 ^a	6	62.8
Layout 2 + 2	1.38 ^a	4.02 ^a	6	62.8
Layout 4 = 4	0.33 ^a	1 ^a	4	125.6

^a Water flow velocity and pressure at one of the laterals. Cross-section area of a lateral is 0.0314 m².^b Maximum overpressure. Isotropic reservoir permeability 1×10^{-14} m².**Fig. 9.** Impact of heat loss from surface to reservoir for injected water and from reservoir to surface for extracted water.

reason for the higher outlet temperature in their study can also be attributed to the less appropriate single-phase assumption used for the gas-filled porous medium model.

The current study shows that the capillary entry pressure has a significant impact on the wetting saturation ratio in the porous medium (Fig. 13c). In particular, the relative permeability of the wetting phase in the vicinity of the injection and extraction wells significantly increases with larger capillary entry pressure. The wetting saturation (injected-water) only reaches 35 % around the extraction well and 45 %

Table 8

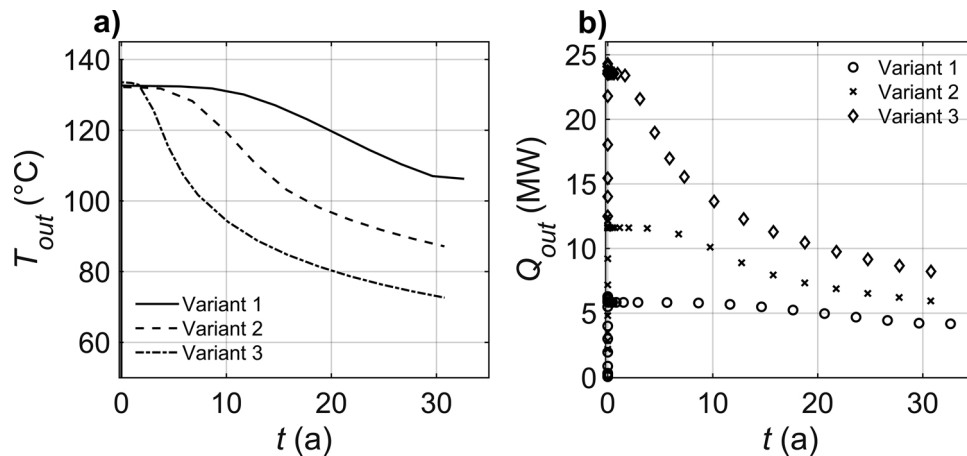
Comparison of thermal output and water injection pressure based on the injected mass flow rate with 2 = 2 laterals.

	Mass flow rate (m s ⁻¹)	Overpressure (MPa)	Average heat extracted from reservoir (MW)
Variant 1	15	2.6 ^a	13.2
Variant 2	30	6 ^a	8.7
Variant 3	60	12.6 ^a	5.2

^a Maximum total injection pressure of laterals.

around the injection well with the capillary entry pressure of 10 MPa. In contrast, the saturation rises to 71 % and 83 % around the extraction and injection wells, respectively, as the capillary entry pressure is decreased to 1 MPa. Aside from this, the wetting saturation ratio ascending with the injected water and with the capillary entry pressure does not enhance the extracted thermal power. Although the lower capillary entry pressure leads to a higher wetting saturation, the injected water cannot further penetrate into the porous medium away from the injection and extraction zone and the heat exchange thus is limited. The reason is that the extraction well simultaneously pumps the water-gas flow from the injection well at the same rate, while the phase saturations reach equilibrium around the injection and extraction wells within a short time.

Relative permeability results shown in Fig. 13d are obtained with the Brooks and Corey (1966) model. The complete displacement of wetting phase is nearly achieved with lower capillary entry pressure. Nevertheless, this displacement is quite limited around the wells due to simultaneous pumping of the extraction well.

**Fig. 10.** Mass flow rate impact on the thermal efficiency of a single-well with 2 = 2 laterals (Fig. 5b). Variant 1: $\dot{m} = 15$ kg s⁻¹, Variant 2: $\dot{m} = 30$ kg s⁻¹ (Base case), Variant 3: $\dot{m} = 60$ kg s⁻¹. Table 5 lists the model parameters for the variants.

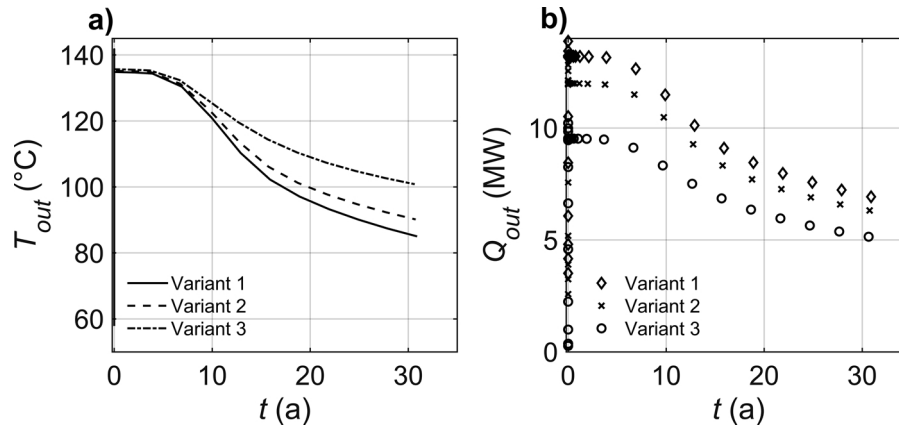


Fig. 11. Injection temperature role on thermal performance of a well with 2 = 2 laterals (Fig. 5b). Variant 1 = 30 °C, variant 2 = 40 °C (Base case), variant 3 = 60 °C. Table 5 delineates the model parameters for the variants.

4. Conclusions

The single-well concept is tested for geothermal efficiency with various scenarios. The model is successfully validated for the single-well geothermal systems. The scenario analysis of the single-well concept with multi-lateral drillings demonstrates that if a target reservoir has an appropriate permeability, the performance of the system can be sustained over long-term extraction periods. In this study, the fixed boundary condition defined at the walls of the models delineate a performance of a single well in a limited reservoir volume. Applying open boundary condition increases the overall performance of a single well by approximately 5 %.

For water-filled porous medium, the single-well system with multiple laterals results in a high thermal output (> 5 MW) and low overpressure (< 10 MPa) if the permeability is isotropic and higher than $5 \times 10^{-15} \text{ m}^2$. Injection into lower permeability formations ($< 5 \times 10^{-15} \text{ m}^2$) can also exceed the maximum sustainable injection pressure. In case, shear failure conditions reach and fractures undergo shear slip that has the potential of triggering seismicity. In contrast, formations with a higher isotropic permeability yield a lower thermal output power due to faster water flow towards the extraction well.

Hence, for configurations with multiple laterals, the vertical spacing between injection and extraction wells is important to avoid thermal or hydraulic breakthrough, and the distance and orientation of the laterals should be adjusted based on the permeability, especially in the vertical direction in case of anisotropic permeability. The higher the porosity and permeability are, the larger is also the ideal well spacing, and the earlier thermal breakthrough may occur. In particular, opposite lateral orientations (2 + 2) between injection and extraction provide satisfactory results in both of the isotropic and anisotropic cases.

For the gas-filled porous medium applications, the capillary entry pressure becomes crucial to drive the saturation and wetting flow to displace the non-wetting phase. However, simultaneous injection and extraction operations cause local saturation of wetting phase around the wells. As a consequence, the injected water cannot penetrate adequately into the reservoir and the heat exchange is limited. In gas-filled porous media, the injection must begin earlier to fill the accessible volume in the reservoir and the extraction should start after a while for sustainable thermal output power.

In future study, wettability alteration by supercritical/gaseous CO_2 injection and its reactivity with minerals can be examined. Moreover, the role of injection temperature on thermal stress and overpressure on

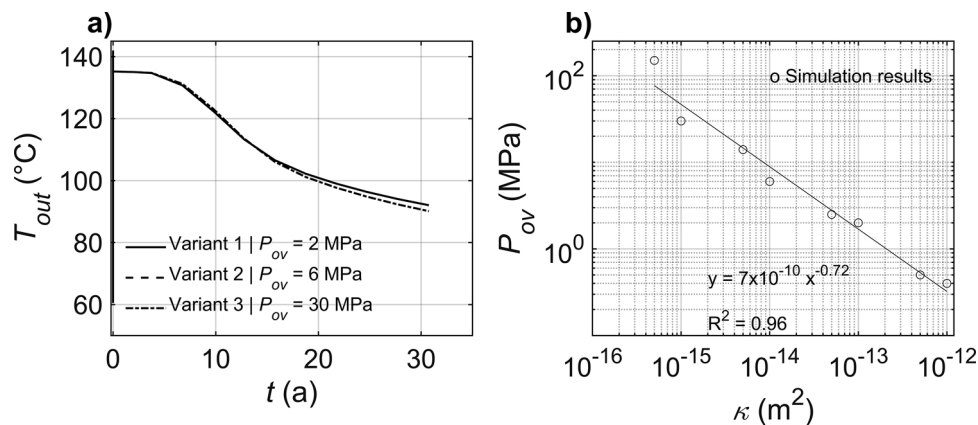


Fig. 12. Permeability (isotropic) effect on the outlet temperature T_{out} and overpressure of a well P_{ov} with 2 = 2 laterals (Fig. 5b). Variant 1, $\kappa = 1 \times 10^{-13} \text{ m}^2$; variant 2 (Base case), $\kappa = 1 \times 10^{-14} \text{ m}^2$; variant 3, $\kappa = 1 \times 10^{-15} \text{ m}^2$. Details of the model parameters for the variants given in Table 5.

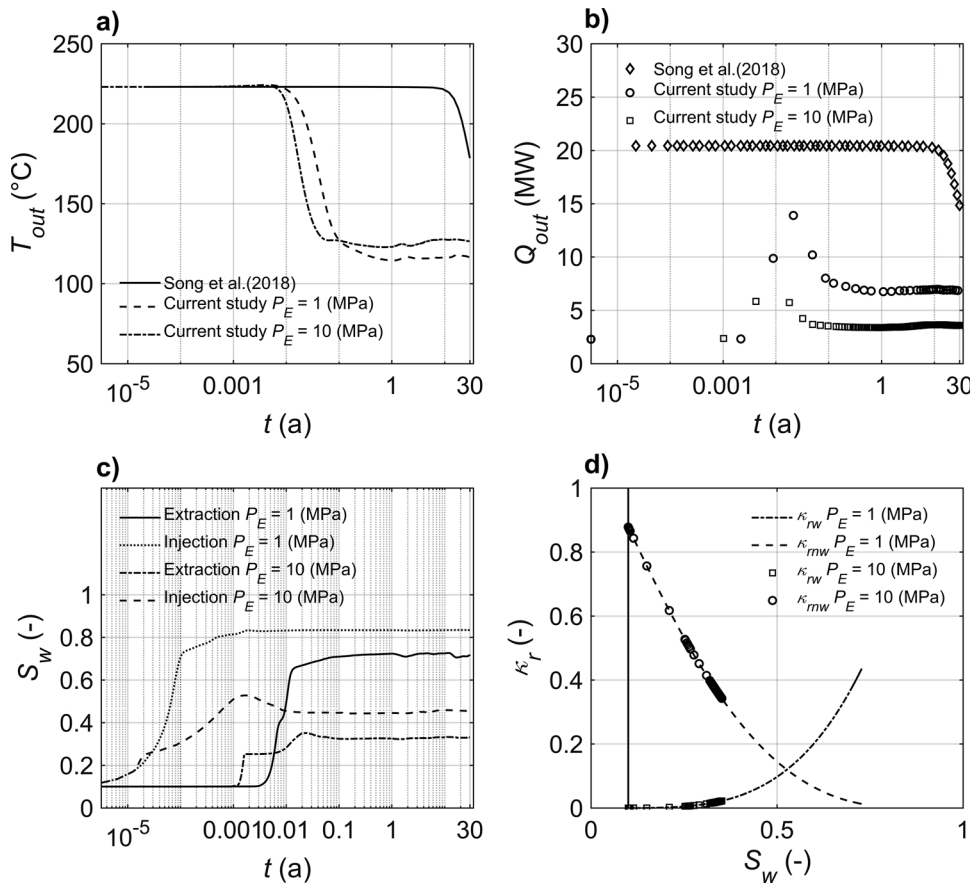


Fig. 13. Comparison of results between the current study and modeling results by Song et al. (2018): a) temperature at outlet, b) thermal output performance, c) wetting saturation (injected water) (S_w) trends over time (initial water saturation is 0.10), d) relative permeability in the vicinity of the extraction well (distance of 1 m). The current study model is applied with two different settings of the capillary entry pressure P_E .

the induced seismicity can be further inspected in geothermal reservoir for single-well systems.

Funding

This research is funded by the internal sources of our institute VITO.

Declaration of Competing Interest

None.

Appendix A

Numerical parameters and the computational times are compared in Table A1 for the different lateral configurations. The auxiliary sweep solution with the ramping parameter, which was applied to the dynamic viscosity to converge to the solution, increased the computation runtime for the stationary solver. For the layout 4 = 4, the number of elements is the largest and its computational runtime was the longest compared to the

Table A1

Comparison of computation runtimes of 3-D anisotropic reservoir model with different lateral layouts (first sub-domain).

Layout	Number of tetrahedral elements solved for		Runtime (s)*	
	Stationary solution for water flow	Time dependent solution for couple heat transfer	Stationary solution for water flow	Time dependent solution for couple heat transfer
No laterals	1,464,285	3,804,572	12,309	1902
2 = 2	1,746,081	4,311,432	4975	3807
2 + 2	1,754,393	4,329,653	3418	3728
4 = 4	3,797,445	8,741,554	6557	10,273

*Hardware specifications: Intel core i7 – 9750H CPU @ 2.60 GHz processor with 16 GB of RAM.

Table A2

Comparison of computation runtimes of 2-D axisymmetric wellbore model (second sub-domain).

Common 2-D axisymmetric wellbore model for all layouts	Number of triangular elements solved for		Runtime (s)*	
	Stationary solution for water flow	Time dependent solution for couple heat transfer	Stationary solution for fluid flow	Time dependent solution for couple heat transfer
Second subdomain	1,807,916	3,986,748	452	778

*Hardware specifications: Intel core i7 – 9750H CPU @ 2.60 GHz processor with 16 GB of RAM.

other layouts. The allocated memory for layout 4 = 4 was nearly 15 GB of RAM.

The number of elements and computational runtime for 2-D axisymmetric wellbore model can be seen in Table A2 and are similar for the 3-D reservoir model due to larger model size ($x = 1000$ m, $z = 4000$ m). The 2-D axisymmetric model allocates nearly 12 GB of RAM. A stationary solution for water flow was considered only in the wellbore system.

References

- Adams, B.M., Kuehn, T.H., Bielicki, J.M., Randolph, J.B., Saar, M.O., 2015. A comparison of electric power output of CO₂ plume geothermal (CPG) and brine geothermal systems for varying reservoir conditions. *Appl. Energy* 140, 365–377. <https://doi.org/10.1016/j.apenergy.2014.11.043>, 140:365–377.
- Assouline, S., 2005. On the relationships between the pore size distribution index and characteristics of the soil hydraulic functions. *Water Resour. Res.* 41 <https://doi.org/10.1029/2004WR003511>. W07019.
- Banks, D., 2009. Thermogeological assessment of open-loop well-doublet schemes: a review and synthesis of analytical approaches. *Hydrogeol. J.* 17, 1149–1155. <https://doi.org/10.1007/s10040-008-0427-6>.
- Bi, G., Li, M., Dou, L., Qu, Z., 2018. Research on structure design and flow field characteristics of the novel jet bit for radial horizontal drilling. *Energy Sci. Eng.* 6, 535–547. <https://doi.org/10.1002/ese3.230>.
- Birner, J., Fritzer, T., Jodocy, M., Savvatis, A., Schneider, M., Stober, I., 2012. Hydraulic characterization of the Malm aquifer in the South German Molasse basin and its impact on geothermal exploitations. *Zeitschrift für Geologische Wissenschaften*. 40 (2), 133–156.
- Blöcher, G., 2016. Report on Radial Jet-drilling (RJD) Stimulation Technology. Project SURE - Grant-Number 654662. <https://doi.org/10.2312/GFZ.6.2.2018.001>.
- Brooks, R.H., Corey, A.T., 1966. Properties of porous media affecting fluid flow. *J. Irrig Drain Div* 92 (2), 61–90.
- Brown, D., 2000. A Hot Dry Rock Geothermal Energy Concept Utilizing Supercritical CO₂ Instead of Water. Proceedings of the Twenty-fifth Workshop on Geothermal Reservoir Engineering, Stanford, California. Stanford University, pp. 24–26 January.
- Büsing, H., Willkomm, J., Bischof, C.H., Clauser, C., 2014. Using exact Jacobians in an implicit Newton method for solving multiphase flow in porous media. *Int. J. Comput. Sci. Eng.* 9 (5/6), 499–508. <https://doi.org/10.1504/IJCSE.2014.064535>.
- Ciriaco, A.E., Zarrouk, S.J., Zakeri, G., 2020. Geothermal resource and reserve assessment methodology: overview, analysis and future directions. *Renewable Sustainable Energy Rev.* 119, 109515. <https://doi.org/10.1016/j.rser.2019.109515>.
- de Marsily, G., 1986. Quantitative hydrogeology: Groundwater Hydrology for Engineers 1st Edition. San Diego, CA, US: Academic Press ISBN-10: 0122089162.
- DiPippo, D., 2016. Geothermal Power Plants: Principles, Applications, Case Studies and Environmental Impact (Fourth Edition). Butterworth-Heinemann, MA, US. <https://doi.org/10.1016/B978-0-08-100879-9.00025-2>.
- Eggertsson, G.H., Lavallée, Y., Kendrick, J.E., Markússon, S.H., 2018. Improving fluid flow in geothermal reservoirs by thermal and mechanical stimulation: The case of Krafla volcano, Iceland. *J. Volcanol. Geotherm. Res.* 106351. <https://doi.org/10.1016/j.jvolgeores.2018.04.008>.
- Evans, K.F., Zappone, A., Kraft, T., Deichmann, N., Moia, F., 2012. A survey of the induced seismic responses to fluid injection in geothermal and CO₂ reservoirs in Europe. *Geothermics* 41, 30–54. <https://doi.org/10.1016/j.geothermics.2011.08.002>.
- Ezekiel, J., Ebigbo, A., Adams, B.M., Saar, M.O., 2020. Combining natural gas recovery and CO₂-based geothermal energy extraction for electric power generation. *Appl. Energy* 269. <https://doi.org/10.1016/j.apenergy.2020.115012>.
- Garapati, N., Randolph, J.B., Saar, M.O., 2015. Brine displacement by CO₂, energy extraction rates, and lifespan of a CO₂-limited CO₂ Plume Geothermal (CPG) system with a horizontal production well. *Geothermics* 55, 182–194. <https://doi.org/10.1016/j.geothermics.2015.02.005>.
- Gossler, M.A., Bayer, P., Zosseder, K., 2019. Experimental investigation of thermal retardation and local thermal non-equilibrium effects on heat transport in highly permeable, porous aquifers. *J. Hydrol. (Amst)* 578, 124097. <https://doi.org/10.1016/j.jhydrol.2019.124097>.
- Gringarten, A.C., Sauty, J.P., 1975. A theoretical study of heat extraction from aquifers with uniform regional flow. *J. Geophys. Res.* 80 (35), 4956–4962. <https://doi.org/10.1029/JB080i035p04956>.
- Huang, W., Cao, W., Jiang, F., 2018. A novel single-well geothermal system for hot dry rock geothermal energy exploitation. *Energy* 162, 630–644. <https://doi.org/10.1016/j.energy.2018.08.055>.
- Huenges, E., 2010. Geothermal Energy Systems: Exploration, Development, and Utilization. Wiley-VCH, Weinheim, Germany, 1st Release. pp. 463. <https://doi.org/10.1002/9783527630479>.
- Kant, M.A., Rossi, E., Duss, J., Amann, F., Saar, M.O., von Rohr, P.R., 2018. Demonstration of thermal borehole enlargement to facilitate controlled reservoir engineering for deep geothermal, oil or gas systems. *Appl. Energy* 212, 1501–1509. <https://doi.org/10.1016/j.apenergy.2018.01.009>.
- Li, T., Shiozawa, S., McClure, M.W., 2016. Thermal breakthrough calculations to optimize design of a multiple-stage enhanced Geothermal System. *Geothermics* 64, 455–465. <https://doi.org/10.1016/j.geothermics.2016.06.015>.
- Likhachev, E.R., 2003. Dependence of water viscosity on temperature and pressure. *Tech. Phys.* 48 (4), 514–515. <https://doi.org/10.1134/1.1568496>.
- Lippmann, M.J., Tsang, C.F., 1980. Ground-water use for cooling: associated aquifer temperature changes. *Ground Water* 18, 452–458. <https://doi.org/10.1111/j.1745-6584.1980.tb03420.x>.
- Lopez, S., Hamm, V., Le Brun, M., Schaper, L., Boissier, F., Cotiche, C., Giuglaris, E., 2010. 40 years of Dogger aquifer management in Ile-de-France, Paris Basin, France. *Geothermics* 39 (4), 339–356. <https://doi.org/10.1016/j.geothermics.2010.09.005>.
- Marx, J.W., Langenheim, R.H., 1959. Reservoir heating by hot fluid injection. *Petr. Trans. AIME* 216, 312–315.
- Menberg, K., Pfister, S., Blum, P., Bayer, P., 2016. A matter of meters: state of the art in the life cycle assessment of enhanced geothermal systems. *Energy Environ. Sci.* 9 (9), 2720–2743. <https://doi.org/10.1039/c6ee01043a>.
- Milnes, E., Perrochet, P., 2013. Assessing the impact of thermal feedback and recycling in open-loop groundwater heat pump (GWHP) systems: A complementary design tool. *Hydrogeol. J.* 21, 505–514. <https://doi.org/10.1007/s10040-012-0902-y>.
- Nader, F.H., Champenois, F., Barbier, M., Adelinet, M., Rosenberg, E., Houel, P., Delmas, J., Swennen, R., 2016. Diagenetic effects of compaction on reservoir properties: the case of early callovian “Dalle Nacrée” formation (Paris basin, France). *Geodynamics* 101, 5–29. <https://doi.org/10.1016/j.jog.2016.05.010>.
- Nair, R., Peters, E., Šliaupa, S., Valickas, R., Petrauskas, S., 2017. A Case Study of Radial Jetting Technology for Enhancing Geothermal Energy Systems at Klaipeida Geothermal Demonstration Plant. Proceedings, 42nd Workshop on Geothermal Reservoir Engineering. Stanford University, Stanford, California, pp. 13–15 February.
- Nicholson, C., Wesson, R.L., 1990. Earthquake Hazard Associated With Deep Well Injection-A Report to the U.S. Environmental Protection Agency. USGS Bulletin no.1951. US Geological Survey, Alexandria, VA, USA.
- Nitschke, F., Held, S., Himmelsbach, T., Kohl, T., 2017. THC simulation of halite scaling in deep geothermal single well production. *Geothermics* 65, 234–243. <https://doi.org/10.1016/j.geothermics.2016.09.009>.
- Peters, E., Blöcher, G., Salimzadeh, S., Egberts, P.J.P., Cacace, M., 2018. Modelling of multi-lateral well geometries for geothermal applications. *Adv. Geosci.* 45, 209–215. <https://doi.org/10.5194/adgeo-45-209-2018>.
- Pruess, K., 2006. Enhanced geothermal systems (EGS) using CO₂ as working fluid—a novel approach for generating renewable energy with simultaneous sequestration of carbon. *Geothermics* 35, 351–367. <https://doi.org/10.1016/j.geothermics.2006.08.002>.
- Randolph, J.B., Saar, M.O., 2011. Combining geothermal energy capture with geologic carbon dioxide sequestration. *Geophys. Res. Lett.* 38 (L10401). <https://doi.org/10.1029/2011GL047265>.
- Revil, A.L., Cathles III, M., Shosa, J.D., Pezard, P.A., de Larouzière, F.D., 1998. Capillary sealing in sedimentary basins: a clear field example. *Geophys. Res. Lett.* 25 (3), 389–392. <https://doi.org/10.1029/97GL03775>.
- Shi, Y., Song, X., Wang, G., McLennan, J., Forbes, B., Li, X., Li, J., 2019. Study on wellbore fluid flow and heat transfer of a multilateral-well CO₂ enhanced geothermal system. *Appl. Energy* 249, 14–27. <https://doi.org/10.1016/j.apenergy.2019.04.117>.
- Song, X., Lv, Z., Li, G., Hu, X., Shi, Y., 2017. Numerical analysis on the impact of the flow field of hydrothermal jet drilling for geothermal wells in a confined cooling environment. *Geothermics* 66, 39–49. <https://doi.org/10.1016/j.geothermics.2016.10.007>.
- Song, X., Shi, Y., Gensheng, Li, Yang, R., Wang, G., Zheng, R., Li, J., Lyu, Z., 2018. Heat extraction performance in enhanced geothermal system with multilateral wells. *Appl. Energy* 218, 325–337. <https://doi.org/10.1016/j.apenergy.2018.02.172>.
- Stauffer, F., Bayer, P., Blum, P., Giraldo, N.M., Kinzelbach, W., 2013. Thermal Use of Shallow Groundwater. CRC Press <https://doi.org/10.1201/b16239>.
- Tester, J.W., Anderson, B.J., Batchelor, A.S., Blackwell, D.D., DiPippo, R., Drake, E.M., Petty, S., 2006. The future of geothermal energy. Massachusetts Institute of

- Technology 358 ISBN: 0-615-13438-6.
- Toews, M., 2019. Method and Apparatus for Power Production. Eavor Technologies Inc. Calgary, Canada, United States Patent Application. 20190154010. .
- Van Genuchten, M.T., 1980. A closed form equation for predicting the hydraulic conductivity of unsaturated soils. *Soil Sci. Soc. Am. J.* 44, 892–898. <https://doi.org/10.2136/sssaj1980.03615995004400050002x>.
- Vilarrasa, V., Carrera, J., 2015. Geologic carbon storage is unlikely to trigger large earthquakes and reactivate faults through which CO₂ could leak. *PNAS* 112 (19), 5938–5943. <https://doi.org/10.1073/pnas.1413284112>.
- Wang, Z., McClure, M.W., Horne, R.N., 2009. A single-well EGS configuration using a thermosiphon. In *Workshop on Geothermal Reservoir Engineering*. Stanford University, Stanford, California.
- Wu, B., Zhang, X., Jeffrey, R.G., Bunger, A.P., Jia, S., 2016. A simplified model for heat extraction by circulating fluid through a closed-loop multiple-fracture enhanced geothermal system. *Appl. Energy* 183, 1664–1681. <https://doi.org/10.1016/j.apenergy.2016.09.113>.
- Zhang, J., Xie, J., Liu, X., 2019a. Numerical evaluation of heat extraction for EGS with tree-shaped wells. *Int. J. Heat Mass Transf.* 134, 296–310. <https://doi.org/10.1016/j.ijheatmasstransfer.2018.12.171>.
- Zhang, L., Gao, C., Ji, B., Zhang, R., Niu, J., 2019b. A simplified assessment method for estimating recoverable geothermal resources. *Geothermics* 79, 145–151. <https://doi.org/10.1016/j.geothermics.2019.01.011>.
- Zhao, J., Tang, C.A., Wang, S.J., 2020. Excavation based enhanced geothermal system (EGS-E): introduction to a new concept. *Geomech. Geophys. Geo-energ. Geo-resour.* 6 (6). <https://doi.org/10.1007/s40948-019-00127-y>.